Jin *et al. Journal of Nanobiotechnology* (2024) 22:619
https://doi.org/10.1186/s12951-024-02908-4

Journal of Nanobiotechnology

RESEARCH **Open Access**

Conformal immunomodulatory hydrogels for the treatment of otitis media

Yuefan Jin[1†], Yueyi Shang[1†], Cuiping Wu[1], Zhengnong Chen[1], Haibo Shi[1], Hui Wang[1*], Linpeng Li[1*] and Shankai Yin[1*]

Abstract
Otitis media (OM), a condition stemming from the proliferation of various bacteria within the tympanic cavity (TC), is commonly addressed through the administration of ofloxacin (OFL), a fluoroquinolone antibiotic. Nevertheless, the escalating issue of antibiotic resistance and the challenge of drug leakage underscore the exploration of an alternative, more effective treatment modality in clinical practice. Here, we introduce a simple and easily implementable fluid-regulated strategy aimed at delivering immunomodulatory hydrogels into the TC, ensuring conformal contact with the irregular anatomical surfaces of the middle ear cavity to more effectively eliminate bacteria and treat OM. This innovative strategy exhibits expedited therapeutic process of antibiotic-resistant, acute and chronic OM rats, and significant reductions in the severity of tympanic membrane (TM) inflammation, residual bacteria within the TC (0.12 $*10^5$ CFU), and the thickness of TM/TC mucosa (17.63/32.43 μm), as compared to conventional OFL treatment (3.6, 0.76 $*10^5$ CFU, 48.70/151.26 μm). The broad-spectrum antibacterial and antibiofilm properties of this strategy against a spectrum of OM pathogens are demonstrated. The strategy is validated to bolster the host's innate immune response through the stimulation of antibacterial protein synthesis, macrophage proliferation and activation, thereby accelerating bacterial eradication and inflammation resolution within the TC. This facile, cost-effective and in vivo degradable technology exhibits promising prospects for future clinical implementation.

Keywords Otitis media treatment, Conformal hydrogels, Innate immune response, Antibiotic-resistant therapy, Fluid-regulated strategy

Introduction

Otitis media (OM), a prevalent inflammatory condition affecting the middle ear (ME), can be triggered by a variety of bacteria, including Gram-positive *S. aureus*, *S. pneumoniae*, or Gram-negative *P. aeruginosa*, *E. coli*, etc. This ailment afflicts approximately 740 million individuals globally each year, with a particularly concerning incidence of 51% among children under the age of 5 [1, 2]. Alarmingly, an estimated 31 million cases of OM with tympanic membrane (TM) perforation are diagnosed annually [3], often leading to recurrent episodes that profoundly impact the physical and psychological well-being of millions due to the conductive hearing impairment. Furthermore, multiple antibiotics, e.g., aminoglycosides,

---

[†] Yuefan Jin and Yueyi Shang contributed equally to this work.

*Correspondence:
Hui Wang
wangh2005@alumin.sjtu.edu.cn
Linpeng Li
lilp@sjtu.edu.cn
Shankai Yin
skyin@sjtu.edu.cn
[1] Shanghai Key Laboratory of Sleep Disordered Breathing, Department of Otolaryngology-Head and Neck Surgery, Otolaryngology Institute of Shanghai JiaoTong University, Shanghai Sixth People's Hospital Affiliated to Shanghai Jiao Tong University School of Medicine, Shanghai 200223, P. R. China

tetracyclines, have been shown to be ototoxic [4, 5], the ototoxic nature of several antibiotics, e.g., aminoglycosides, tetracyclines, etc., has significantly limited the available treatment options for OM. Conventional clinical approaches for managing OM encompass the use of aqueous drops, oral antibiotics, etc., with the instillation of the fluoroquinolone antibiotic ofloxacin (OFL) into the tympanic cavity (TC) being the prevailing method due to its convenience and cost-effectiveness [6]. Nonetheless, the therapeutic efficacy of OFL is hampered by several challenges: the misuse of antibiotics fosters the development of protective biofilms and antibiotic-resistant strains [7], complicating bacteriostasis within the TC; moreover, the high fluidity of the drug solution leads to its drainage through perforated TM or the eustachian tube (ET), limiting its contact with the bacterial colony and reducing its antibacterial potency [8]. Hence, there is an urgent imperative to devise a non-antibiotic and customizable treatment strategy to combat diverse bacteria, particularly antibiotic-resistant strains, in the context of OM.

The escalating issue of antibacterial resistance among pathogenic bacteria poses a formidable obstacle to effective OM therapy. Bacteria possess the intrinsic ability, derived from aeons of competition, to evolve rapidly through mutations and transfer of DNA through horizontal gene transfer to overcome the threat posed by antibiotics that act on bacteria by targeting essential survival processes such as inhibiting cell-wall synthesis and interfering with the synthesis of vital proteins, DNA and RNA [9]. In light of this, antimicrobial peptides, such as ε-poly-L-lysine [10], have emerged as promising alternatives to antibiotics due to their broad-spectrum antibacterial activity and reduced propensity for resistance development, attributed to their ability to disrupt microbial membranes through their unique amphiphilic structure and polycationic headgroups. However, challenges persist in the extraction and cost-effective production of these peptides for in vivo applications [11]. Similarly, inorganic nanomaterials, like silver nanoparticles (Ag NPs), graphene, and MXene, have shown promise in overcoming antibiotic resistance by virtue of their distinctive physicochemical properties, which enable them to bind to and disrupt bacterial membranes, causing leakage of cytoplasmic components [12–15]. Despite their efficacy, the non-biodegradability and documented toxicity of these materials constrain them in vivo utility [16]. Natural polymers, particularly chitosan (CS), exhibit remarkable biocompatibility, biodegradability, and antibacterial efficacy due to their positively charged amino and hydroxyl groups [17–19], which interact electrostatically with bacterial membranes. In addition to its broad-spectrum antibacterial activity, chitosan demonstrates a high bactericidal rate and disrupts bacterial biofilms effectively, reducing the risk of bacterial resistance emerging from incomplete eradication. These attributes enhance its potential to combat resistant infections. Given these advantages, chitosan holds significant promise for advancing current treatment strategies for bacterial otitis media, transitioning from experimental research to clinical application. However, its limited fluidity and infiltration capacity in aqueous solutions at effective concentrations have impeded its widespread adoption as ear drops in the clinical management of otitis media.

The persistence of OM stems from the challenge of thoroughly eradicating bacteria within the enclosed and intricate TC, impeding the healing of the TM and potentially leading to severe complications like meningitis and cholesteatoma [20]. Thus, there is a pressing need to develop a drug delivery system that can remain in the TC without drainage, offering a promising avenue for efficient treatment. In a recent study, Chen et al. introduced a magnetic system for delivering hydrogel microrobots into the inner ear, leveraging magnetic attraction to prolong the retention of hydrogels in vivo [21]; however, challenges remain regarding the non-metabolism and the logistical complexities associated with external magnet utilization. Fortunately, stimulus-responsive hydrogels, which can adjust their viscosity or mechanical properties in response to stimuli like heat, light, or pH, hold potential as drug carriers for OM treatment due to their fluid-regulating properties.

In this context, we propose an alternative fluidity-regulated strategy (FRS) for formulating bioabsorbable thermoresponsive hydrogels that leverage the temperature differential between the human body and the environment for the effective treatment of otitis media (OM). This strategy, utilizing the cost-effective and biocompatible Pluronic F127 and chitosan (CS), exhibited remarkable antibacterial efficacy (93.8% at day 7) in vivo against antibiotic-resistant *S. aureus* and other common OM pathogens, including *S. pneumoniae*, *E. coli*, and *P. aeruginosa*. Compared to conventional non-FRS treatments, FRS significantly accelerated the healing of perforated tympanic membranes, enhanced antibacterial efficacy in the tympanic cavity, and prevented thickening of the tympanic membrane and middle ear mucosa. This was achieved through prolonged and conformal contact with bacterial colonies adhering to the recesses of the irregular anatomical structure of the tympanic cavity [22, 23]. Furthermore, using a chronic OM rat model, we validated the enhanced therapeutic efficacy of FRS, as demonstrated by restored vestibular function, confirmed via micro-computed tomography (micro-CT) and behavioral assessments. Notably, the auditory brainstem response (ABR) threshold in FRS-treated rats was markedly lower than in other groups, indicating superior hearing recovery with FRS. Additionally, we elucidated the molecular mechanisms underlying FRS-mediated modulation of antibacterial activity in vivo, revealing its capacity to induce the expression of antimicrobial proteins *Reg3g* and components of the BPI fold-containing family B, and regulate genes associated with macrophage activity *Csf2*, *Cd14*, and *Nos2*, thereby bolstering the host's innate immune response against bacteria. The FRS drug exhibits a compelling combination of cost-effectiveness, efficacy, ease of administration, and biodegradability, holding immense promise for the clinical management of OM.

Result and discussion

Principle and design of FRS for the treatment of OM

Ordinarily, the use of OFL ear drops prevails in clinical practice due to their potent antimicrobial efficacy and cost-effectiveness. However, as depicted in Fig. 1a, the high fluidity of OFL leads to the leakage through the tympanic membrane (TM) or eustachian tube (ET), resulting in suboptimal bactericidal efficacy and a heightened recurrence rate. Moreover, conventional injectable non-FRS hydrogels often exhibit inadequate conformal ability, forming numerous air gaps between the gel and TC mucosa. Hence, we opted for stimuli-responsive FRS hydrogels comprising FDA-approved CS and Pluronic F127 as injectable antibacterial agents for OM treatment. These innovative hydrogels facilitate the effective delivery of antibacterial agents into the TC, transitioning between a flowing injectable state in vitro and a non-flowing state in vivo, thereby ensuring prolonged and conformal contact with the bacterial colony within the TC mucosa, especially in intricate areas, and complete biodegradation and assimilation in vivo.

The FRS hydrogel showcases exceptional topological conformal properties attributable to its in vivo phase transition, enabling it to flow into and adhere to bumpy corners and TC mucosa. To validate this feature, FRS hydrogel was applied to curved pig epidermis at a low temperature to mimic ear conditions. As illustrated in Fig. 1b, numerous air gaps were observed between the CS hydrogel and the curved epidermis, whereas FRS tightly adhered to the surface due to its phase transition characteristics. Similarly, FRS hydrogel exhibited superior fluidity, enabling it to penetrate tiny corners of a customized mold, unlike non-FRS CS hydrogel, which faced limitations due to high viscosity (Fig. S1a).

The FRS hydrogel formulation primarily consists of thermosensitive Pluronic F127 and biocompatible antibacterial components, which undergo gelation in vivo due to the near-body temperature lower critical solution temperature (LCST) of the Pluronic F127 triblock copolymers (Fig. 1c). While various antibacterial additives have been explored recently [24–28], including inorganic nanoparticles and organic polypeptides, we advocate for CS due to its high antibacterial efficacy (approximately 90%), widespread availability, and cost-effectiveness (0.016 $/mL), along with its broad-spectrum antibacterial properties against Gram-positive, Gram-negative, and antibiotic-resistant strains. In contrast, emerging alternatives like MXene, polypeptides, and Ag NPs, which have similar antibacterial efficiencies, involve significantly higher costs [14, 29–43]. Additionally, commonly used clinical ofloxacin ear drops (purchased from a pharmacy in Shanghai, China) are priced at 0.63 $/mL, which is eight times higher than the cost of FRS (0.07 $/mL), as shown in Fig. 1d and Fig. S3.

The tunable fluidity was assessed through rheological analysis. FRS hydrogel transitions from a fluidic state at low temperatures to a gel-like consistency at body temperature, facilitated by reversible alterations in hydrophobicity and intermolecular hydrogen bonding interactions [29], showcasing thermally responsive and reversible sol-gel transition properties (Fig. 1e). Different concentrations of CS in FRS hydrogels modulate their fluidity, impacting topological conformal properties (Fig. S1b). The gelation time of FRS hydrogels in the TC was within minutes and varied based on CS content, with higher concentrations impeding fluidity and antibacterial efficacy within the enclosed TC (Fig. S1c, S1d), as evidenced in Fig. S2. The rheological properties of various FRS hydrogels were thoroughly analyzed in response to temperature fluctuations to confirm the temperature-regulated reversible sol-gel transition (Fig. 1f and g, S1e). Except for the neat CS hydrogel, all mixed hydrogels exhibited temperature-sensitive changes in storage modulus (G') and loss modulus (G"), as evidenced by a decrease in tanδ (G"/G') to below 1 and an increase in loss modulus with rising temperatures. These rheological characteristics enable the FRS to be administered at room temperature by dripping the liquid formulation through the external auditory canal, where it naturally flows into the middle ear cavity under the influence of gravity, achieving uniform distribution due to its excellent fluidity. Upon reaching body temperature, the hydrogel undergoes a sol-to-gel phase transition, ensuring positional stability and preventing leakage from body movements, thereby providing prolonged therapeutic effects.

Therapeutic efficacies of FRS hydrogels on antibiotic-resistant OM treatment

Antibiotic resistance poses a significant challenge to effective antibacterial therapy in the present era, diminishing bacteriostatic efficacy. This issue is particularly pronounced in the treatment of OM, where the ototoxicity of aminoglycosides, tetracyclines, and other antibiotics has limited the available treatment options. To address

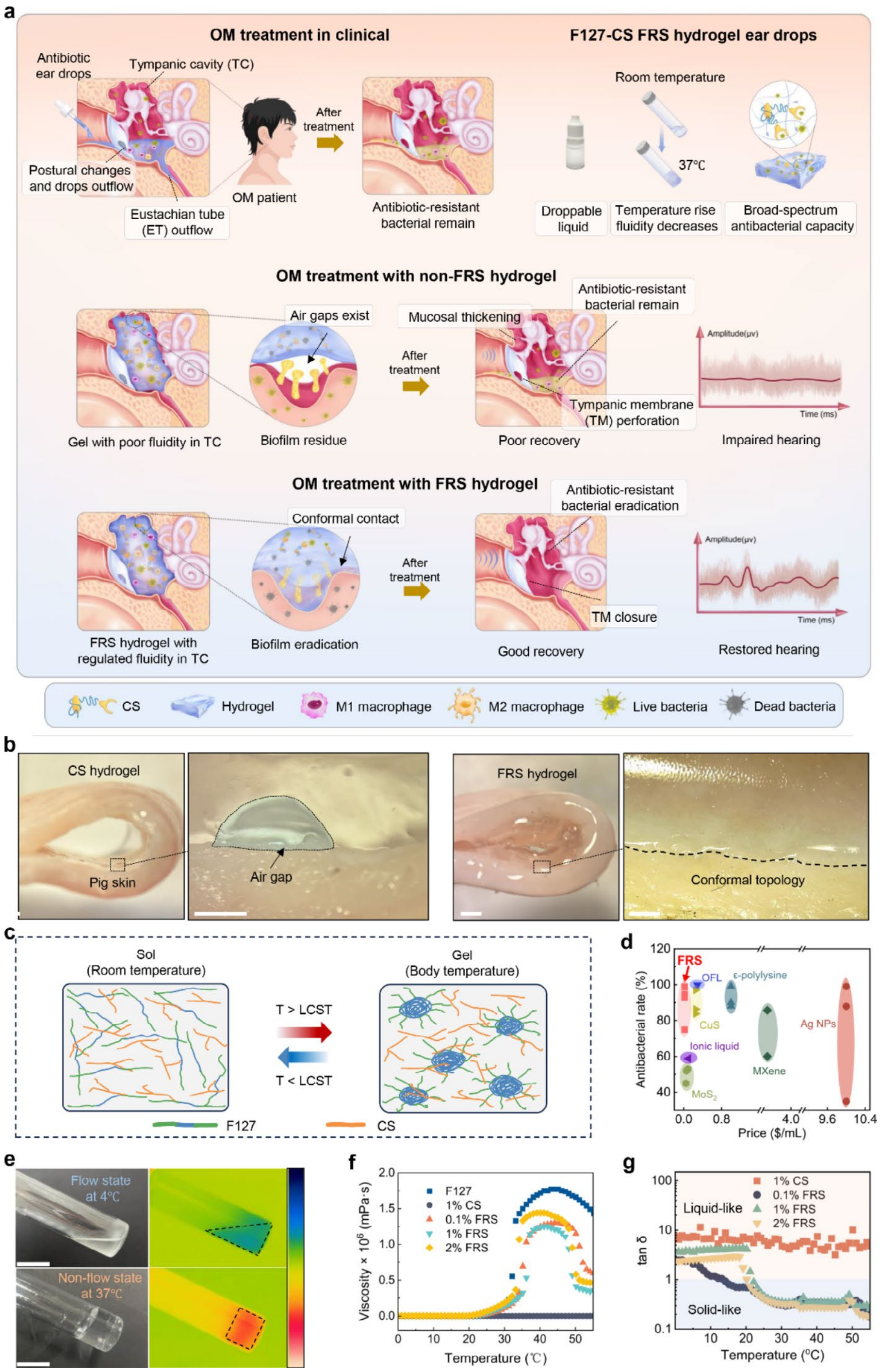

Fig. 1 Illustration and property of FRS hydrogels in the treatment of OM disease. (**a**) Schematic illustration of FRS in the ME. Traditional strategy is usually accompanied by a fluid drainage of antibiotic aqueous solution through TM or ET. CS hydrogel cannot stay in adequate contact with bacterial colonies and biofilms. FRS hydrogel in this work eliminates multiple bacterial, especially antibiotic-resistant bacteria, in the enclosed TC and restores its hearing. (**b**) Representative photographic of normal CS hydrogel and FRS hydrogel on the curved ME mucosa, showing the existence of air gaps and conformal topology, respectively (scale bar: 5 mm, 500 μm). (**c**) Schematic illustration of the phase transition mechanism of the FRS hydrogels. (**d**) Plot of the reported antimicrobial biological additives based on their price of raw materials and reported antibacterial rate. FRS, inorganic copper sulfide (CuS), silver nanoparticles (Ag NPs), molybdenum disulfide nanosheets (MoS$_2$), MXene, polypeptide ε-polylysine, antibiotics OFL, ionic liquid. (**e**) Photographs and infrared camera images of FRS hydrogels at body temperature (37℃) and low temperature (4℃), demonstrating the transition between fluidic state at low temperature and solid-like gel state at body temperature (scale bar: 2 cm). (**f**) The viscosity and (**g**) the calculated tanδ (*G″/G′*) of FRS hydrogels with different recipes at a temperature sweep from 0℃ to 55℃, showing the sol-gel transition

this, we conducted a comprehensive evaluation of FRS's antibacterial efficacy against antibiotic-resistant bacteria in vivo (Fig. 2). OFL-resistant *S. aureus* was selected as the pathogen due to the widespread use of OFL in clinical OM management. Control groups included a blank control (CON), 1% w/v CS, and 0.3% w/v OFL, while FRS hydrogels with varying CS concentrations (0.1%, 1%, and 2% w/v) and FRS-OFL with 0.3% w/v OFL were also examined. Notably, the impact of conformal contact was assessed by comparing the healing outcomes of the OFL and FRS-OFL groups, as well as the CS and 1%FRS groups.

An OFL-resistant OM model was established by injecting OFL-resistant *S. aureus* into the ME (Fig. 2a), with therapeutic efficacy evaluated through quantitative assessments of TM healing, residual bacteria in the ME, and TM and mucosal thickness across different groups (Fig. 2b and c). Otoscopy was employed to visually assess TM recovery, revealing that FRS significantly expedited TM healing post OFL-resistant *S. aureus* infection. Notably, the perforated TM treated with 1%FRS displayed transparent closure by day 7, devoid of significant tissue proliferation. In contrast, TMs treated with CS or OFL exhibited persistent perforation or closure with evident inflammation, edema, and suppuration, starkly differing from the normal lamina propria structure. The FRS-OFL treated TM showcased transparent closure with radial vascularity and congestion. Hematoxylin and eosin (H&E) staining further confirmed the superior healing outcomes of 1%FRS, as evidenced by a significantly reduced TM thickness (17.63±7.44 μm) compared to CS (67.65±18.32 μm), OFL (48.70±9.12 μm), and FRS-OFL (34.36±4.77 μm) groups, aligning more closely with normal rat TM thickness (10.08±6.39 μm). Additionally, we assessed the condition of the observed TM based on four parameters: TM closure, vascular proliferation, secretion, and TM thickening and fibrosis, with a scoring system where 0 denotes a return to normal, 1 signifies incomplete recovery, and 2 indicates no significant improvement. Notably, the healing outcomes for the 1%FRS group (8.6±1.7 healing days, severity score of 1.0±0.71) were markedly superior to those of the CS (13.6±1.8 healing days, severity score of 6.2±1.10), OFL (12.8±2.0 healing days, severity score of 3.6±1.14), and FRS-OFL (12±2.2 healing days, severity score of 2.6±1.14) groups. These findings underscore the optimal healing condition achieved with 1%FRS treatment of the TM.

Subsequently, bacteria were extracted from the ME under sterile conditions to quantify colony-forming units (CFU). Remarkably, 1%FRS exhibited the lowest colony count (0.12±0.05 $*10^5$ CFU), while CS (1.57±0.19 $*10^5$ CFU), OFL (0.76±0.16 $*10^5$ CFU), and FRS-OFL (0.60±0.15 $*10^5$ CFU) groups displayed approximately 13, 6, and 5 times higher CFU counts, respectively. The antibacterial efficiency of 1%FRS and OFL against OFL-resistant *S. aureus*, calculated based on CFU differences relative to the CON group, stood at 93.8% and 60.8%, respectively, underscoring the superior bacteriostatic properties of 1%FRS against antibiotic-resistant OM.

Furthermore, surgical removal of rat bullae enabled the observation of inflammatory responses. Notably, the ME mucosa in untreated, OFL, and CS groups exhibited marked edema and thickening (Fig. 2b), accompanied by increased inflammatory cell infiltration. In contrast, FRS-OFL and 1%FRS groups displayed mucosal characteristics closer to normal, with intact epithelium and reduced edema. Quantitative analysis further revealed that the mucosa in the 1%FRS group (32.43±7.44 μm) was close to the normal rat mucosal thickness (21.5±3.53 μm) [30], when those of CS (319.05±30.72 μm), OFL (151.26±32.19 μm) and FRS-OFL (80.09±25.35 μm) were highly edematous, indicating superior therapeutic effects in OFL-resistant rats.

It is noteworthy that the bacteriostatic activity of the 2%FRS group was less effective than the 1%FRS groups in vivo (Fig. S4a and S4b), despite CS being the primary bactericidal agent in the mixed gel. The healing days (13.6±1.14 days), TM thickness (57.81±8.73 μm), the severity score of recovered TMs (5.4±1.1), residual bacteria in ear (0.99±0.20 $*10^5$ CFU) and mucosa thickness (109.44±19.79 μm) of 2%FRS, were generally worse than those of 1%FRS. The inferior outcomes of the 2%FRS group were attributed to its increased viscosity (3324 mPa·s, almost 4 times higher than that of 1%FRS), which hindered topological conformal properties in the TC, emphasizing the critical role of hydrogel fluidity in antibacterial performance in vivo.

The inflammatory response of ME mucosa at day 7 was characterized by quantifying the M2/M1 macrophage ratio through immunofluorescent staining. CD206, a M2 macrophage marker shown in green, of 1%FRS group was clearly more than that of CON group (Fig. 2d), indicating the presence of more reparative M2 phenotypes. Notably, the 1%FRS group (2.54±0.64) exhibited a significantly higher M2/M1 ratio than the CON group (0.63±0.10), indicative of a more reparative inflammatory response.

To further explore the inhibitory effects of 1%FRS on the proliferation of OFL-resistant *S. aureus*, antibacterial properties and biofilm integrity were assessed in vitro by 6 h incubation and subsequently direct live/dead staining (direct fluorescence method) or diluted and incubated for an additional 24 h (spread-plate method). As shown in Fig. 2e, 1%FRS demonstrated superior bacteriostatic behavior against antibiotic-resistant *S. aureus* compared to OFL and F127. As calculated in Fig. S4c and S4d, the antibacterial efficiencies of 1%FRS were notably higher (73.48±3.30% of direct fluorescence method and 69.38±7.19% of spread-plate method) than those

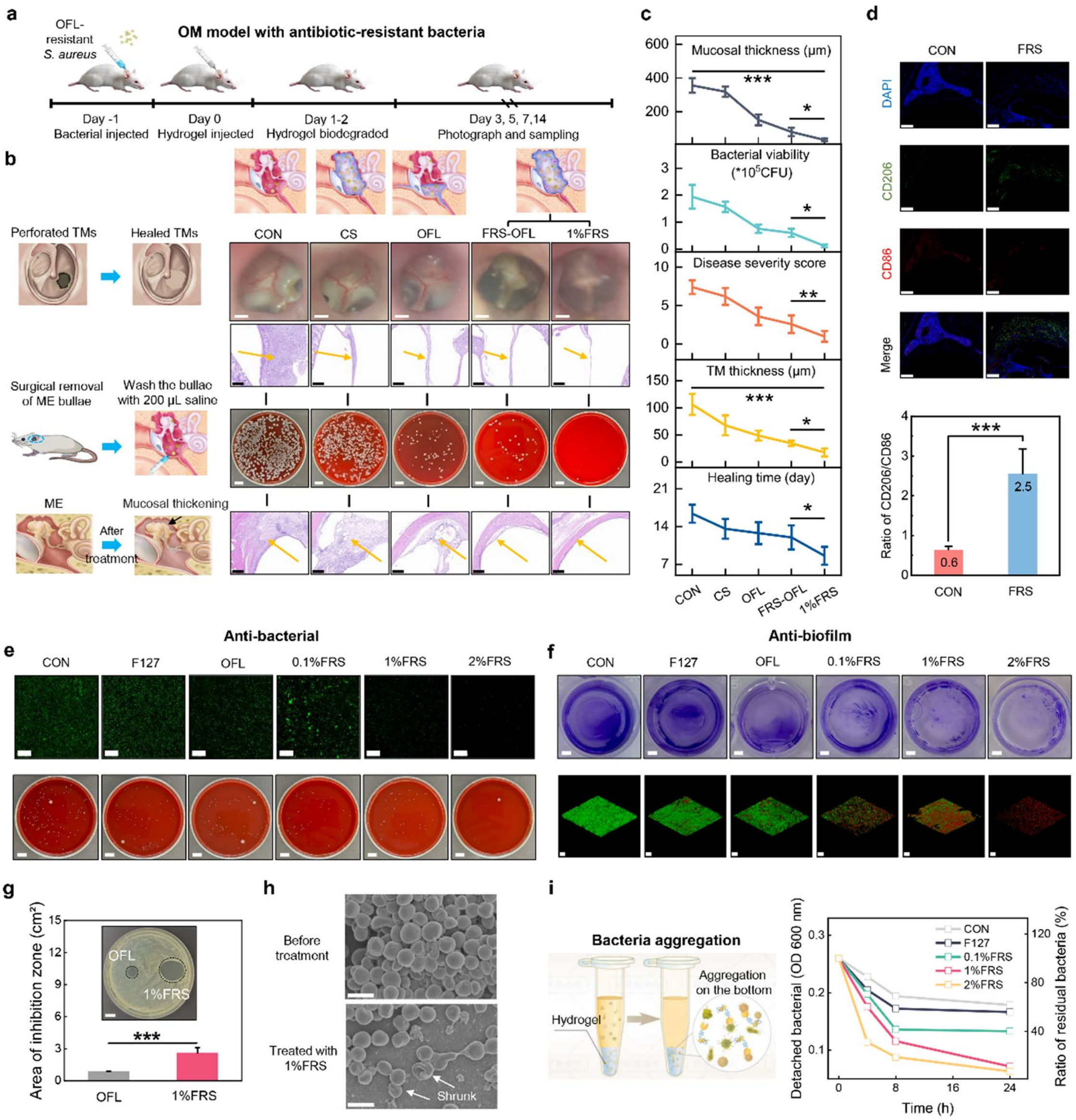

Fig. 2 The therapeutic effect of FRS hydrogels on antibiotic-resistant OM. (**a**) Schematic representation showing the procedure of the establishment and treatment of antibiotic-resistant OM rat. (**b**) Schematic diagram and representative photographic images of the recovered TMs at different degrees of closure and transparency at day 7 (scale bar: 500 μm), cultured bacteria at day 7 by washing the surgical removed ear bullae with saline (scale bar: 1 cm), and calculated thickness of TMs (scale bar: 200 μm) and ME mucosa (scale bar: 200 μm) at day 7 of different groups, including CON, F127, OFL, and two FRS groups. (**c**) The corresponding statistical data according to the above photos, including the observed healing days required for the closure of perforated TMs; the quantitative score of recovered TMs at day 7 in terms of the observed TMs closure, vascular proliferation, secretion, TMs thickening and fibrosis; the statistic bacteria viability in TC at day 7; the counted TM and mucosal thickness of different groups at day 7. (**d**) Immunofluorescence staining of CD206 (green), CD86 (red), and nuclei (blue) of untreated OM rats (CON) and 1%FRS-treated rats (scale bar: 200 μm), and their corresponding quantification of the ratio of CD206 to CD86. (**e**) The anti-bacterial and (**f**) anti-biofilm properties of different groups against OFL-resistant bacteria in vitro, including CON, F127, OFL, FRS. Fluorescence staining (scale bar: 100 μm) and spread-plate culture photos after 1 day (scale bar: 1 cm) of residual OFL-resistant *S. aureus* treated by different groups. The variation of OFL-resistant *S. aureus* biofilm by stained with crystal violet (scale bar: 2 mm), or propidium iodide (PI) and Syto-9 (scale bar: 100 μm). (**g**) The statistical chart and image of inhibition zone of OFL and 1%FRS groups (scale bar: 1 cm). (**h**) Representative SEM images of OFL-resistant *S. aureus* morphologies before and after FRS treatment (scale bar: 1 μm), where shrunk membrane can be observed. (**i**) The schematic diagram of bacteria aggregation experiment and its calculated detached bacterial of different groups. All statistical analyses were performed by one-way ANOVA, data represent mean ± standard deviation, *$p < 0.05$, **$p < 0.01$, ***$p < 0.001$

of OFL (59.76±15.11%, 37.01±11.00%) and F127 group (53.96±9.52%, 12.32±0.43%), underscoring its excellent bacteriostatic properties.

Eradication of bacterial biofilms is critical to prevent recurrence of OM. The antibiofilm properties of FRS against OFL-resistant *S. aureus* were confirmed through crystal violet staining (Fig. 2f), demonstrating the disruption of biofilms. The 3D reconstructions of live/dead staining of the bacterial biofilms were stained by Syto9/PI and observed by confocal laser scanning microscopy (CLSM), where the red fluorescence suggested an increase in the dead bacteria of different groups. Through statistics (Fig. S4e and S4f), crystal violet stained biofilm masses in 1%FRS (0.38±0.09) were much less than that of OFL (0.86±0.04), and fluorescence intensity of Syto9/PI stained dead bacteria in 1%FRS (73.83±7.21) was approximately 6 times higher than that of OFL (11.66±3.58), highlighting the efficacy of 1%FRS in disrupting OFL-resistant *S. aureus* biofilms.

Additionally, the inhibition zone of 1%FRS and OFL against OFL-resistant *S. aureus* was assessed (Fig. 2g), with 1%FRS (2.56±0.53 cm^2) exhibiting a significantly larger inhibition zone area than that of OFL (0.84±0.06 cm^2). SEM imaging in Fig. 2h further revealed the altered morphology of OFL-resistant *S. aureus* post-treatment with 1%FRS. Moreover, bacterial aggregation assays highlighted the enhanced capacity of different hydrogels to absorb OFL-resistant *S. aureus*, with 1%FRS displaying superior adsorption capabilities. After conversion (Fig. 2i), the ratio of residual OFL-resistant *S. aureus* in 1%FRS solution at 24 h (11.17%), significantly lower than those of F127 (55.82%) and CON groups (61.64%), demonstrating the excellent adsorption capacity of 1%FRS.

Accelerated therapy of OM by conformal contact

To further illustrate the enhanced effectiveness of conformal contact in the treatment of OM, we established an acute OM model using *S. aureus* (Fig. 3b). Images of TMs in Fig. 3a and S5a reveal that TMs treated with CS still exhibited significant pathological changes, while those treated with OFL were mostly healed but with accompanying fibrosis, thickening, and vascular proliferation. In contrast, TMs treated with FRS-OFL and 1%FRS showed almost complete recovery, with only slight residual fibrosis at the perforation site. Statistically, as show in Fig. 3c and S5b, the average healing time of the FRS groups (7.6±1.5 days for FRS-OFL, 8.0±2.0 days for 1%FRS) was significantly shorter than that of the non-FRS groups (11.6±2.0 days for OFL, 14.6±2.7 days for CS), as well as the F127 group (14.8±2.5 days). The TM thickness in the FRS groups (14.07±4.46 μm for FRS-OFL, 21.56±13.02 μm for 1%FRS) was also lower than that in the control groups (36.04±8.55 μm for OFL, 102.46±17.45 μm for CS), shown in Fig. 3e. The quantitative severity score of TMs treated with FRS-OFL (1.2±0.4) and 1%FRS (1.2±0.8) was notably lower than that of OFL (3.2±0.8) and CS (5.2±0.8), indicating the role of FRS in accelerating TM healing.

Following that, we isolated bacteria from the treated ME. On blood agar plates, the FRS groups displayed minimal colonies on day 7, whereas the CON, CS, and OFL groups still had a substantial number of colonies visible. As illustrated in Fig. 3d and S5c, 1%FRS (0.27±0.15 *10^5 CFU on day 5, 0.05±0.07 *10^5 CFU on day 7) and FRS-OFL (0.51±0.26 *10^5 CFU on day 5, 0.14±0.12 *10^5 CFU on day 7) exhibited the fewest colonies, while OFL (2.11±1.11 *10^5 CFU on day 5, 0.24±0.25 *10^5 CFU on day 7) and CS (5.86±2.31 *10^5 CFU on day 5, 1.02±0.59 *10^5 CFU on day 7) were nearly 5 and 10 times higher, respectively, underscoring the superior antibacterial efficacy of FRS in vivo.

H&E staining of the ME mucosa revealed that the ME mucosa affected by OM was significantly edematous (266.81±48.60 μm). Similarly, the ME mucosa thickness in the 1%FRS group (36.56±13.42 μm) was notably thinner than that in the CS group (261.86±56.12 μm), as well as in the OFL group (116.54±13.51 μm) and FRS-OFL group (62.19±19.98 μm). Furthermore, the analysis of the cell per unit area of the ME mucosa, as depicted in Fig. S5d, indicated a significantly lower cell count in the 1%FRS group compared to the control group, suggesting reduced inflammatory proliferation and exudation. As shown in Fig. S6, 2%FRS was also found to be less effective than 1%FRS in vivo. Parameters such as TM healing days (11.4±0.4 days), quantitative score of recovered TMs (4.2±1.1), residual bacteria in the ear (0.23±0.14 *105 CFU on day 7), TM thickness (79.88±9.37 μm), and mucosa thickness (101.34±15.28 μm) were generally poorer than those of 1%FRS.

The inflammatory response of the ME mucosa was characterized by quantitatively analyzing macrophages and inflammatory factors. Macrophages, crucial immune cells influencing wound healing, can transition into pro-inflammatory M1 or reparative M2 phenotypes to regulate inflammation or promote tissue repair, respectively. Immunofluorescence analysis and quantitative results in Fig. 3f and g, and S7 indicated that the 1%FRS group had a higher M2/M1 ratio (2.15±0.76) compared to the control group (0.30±0.07), suggesting a higher proportion of M2 macrophages that can prevent the progression from acute OM to chronic OM, signifying recovery in the FRS group while inflammation persisted in the CON group. Furthermore, the expression of inflammatory factors analyzed through immunohistochemistry (Fig. 3h and i) demonstrated that the levels of interleukin-1β (IL-1β) and interleukin-6 (IL-6) in the 1%FRS group (0.14±0.01, 0.16±0.02) and FRS-OFL group (0.10±0.03, 0.12±0.02) were significantly lower than those in the OFL group

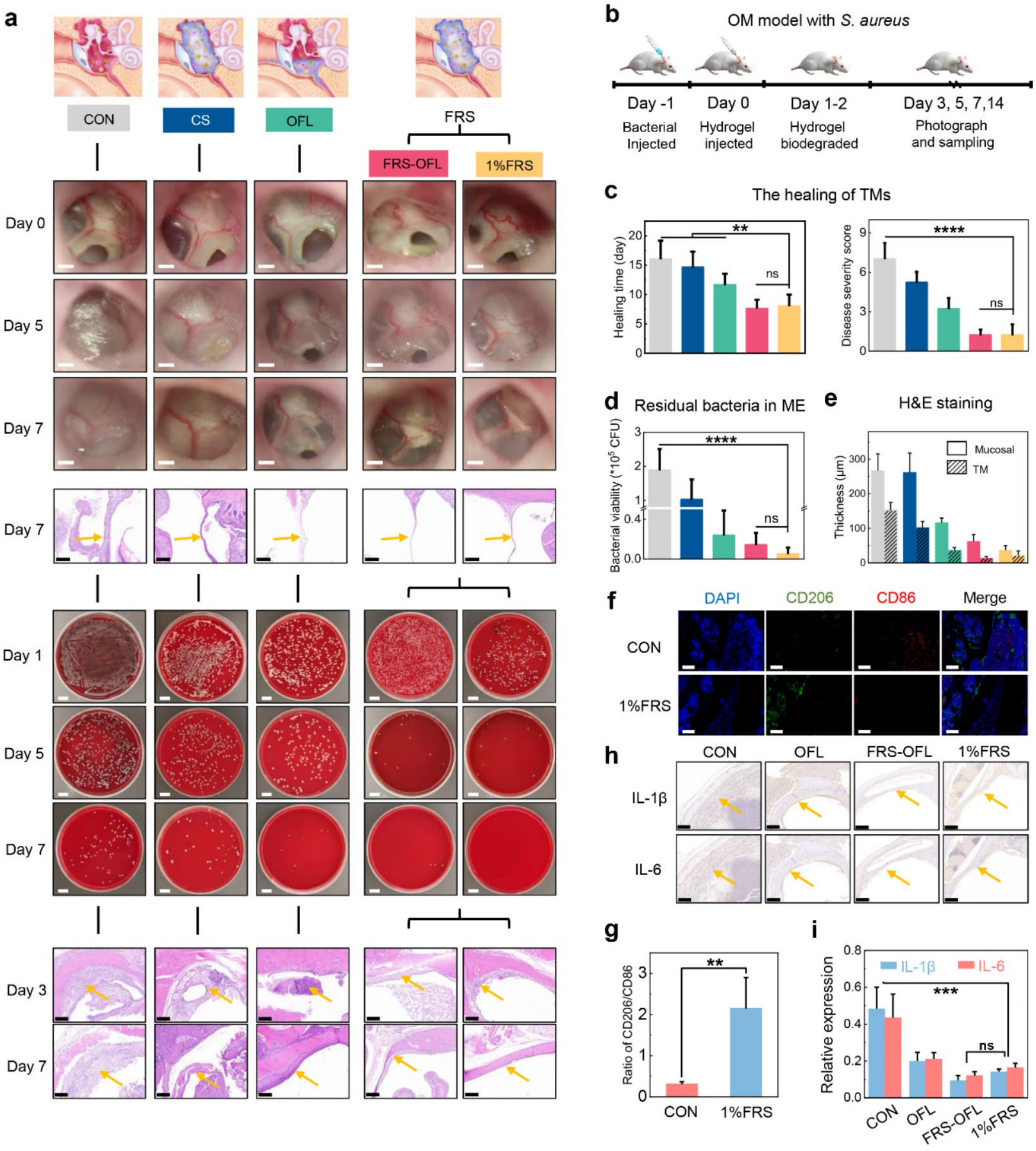

Fig. 3 Accelerated therapy of OM by FRS in vivo. (**a**) Representative images of recovered TMs, cultured residual bacteria, ME mucosa of different treatment groups, including CON, CS, OFL and two FRS groups. Photos of recovered TMs in different degrees of closure and transparency (scale bar: 500 μm), as well as different thickness (scale bar: 200 μm), cultured residual bacteria in ear by washing the surgical removed ear bullae with saline (scale bar: 1 cm), and H&E staining of the mucous membrane lining the ear bulla (scale bar: 200 μm) were shown. (**b**) Schematic representation showing the procedure of the establishment and treatment of OM rat. (**c**) The observed number of days required for the closure of perforated TMs, and the quantitative score of recovered TMs at day 7 in terms of the observed TMs closure, vascular proliferation, secretion, TMs thickening and fibrosis. (**d**) The corresponding statistic residual bacteria viability at day 7. (**e**) The corresponding statistic mucosal and TM thickness of different groups at day 7. (**f**) Immunofluorescence staining of CD206 (green), CD86 (red), and nuclei (blue) of untreated and 1%FRS treated rats, and (**g**) their corresponding quantification of the ratio of CD206 to CD86. (**h**) Immunohistochemistry staining of IL-1β, IL-6 in the ME mucosa of different treatment groups and (**i**) their corresponding statistic expression. All statistical analyses were performed by one-way ANOVA, data represent mean ± standard deviation, ns > 0.05, $**p < 0.01$, $***p < 0.001$, $****p < 0.0001$

(0.20 ± 0.05, 0.21 ± 0.03) and CON group (0.48 ± 0.12, 0.43 ± 0.13), indicating that the rats treated with 1%FRS had markedly lower inflammation levels and comparable recovery to conventional OFL ear drops treatment.

FRS could be metabolized in vivo, which was demonstrated through observation of TC after FRS injection. As shown in Fig. S8a and b, FRS hydrogel was completed dissolved in PBS at 37℃, and no FRS was observed in the surgically removed TC. Intraepidermal injection was used to watch the metabolic processes of FRS (Fig. S8c). Over time, the bulge was gradually diminished, suggesting the absorption of FRS in vivo.

Therapeutic efficacies of FRS on chronic OM rats

The therapeutic efficacy of antibacterial drugs on a chronic OM model holds significant clinical relevance due to the challenge of eradicating persistent bacterial colonies. In this study, we established a chronic OM model following a previously reported protocol (Fig. 4a) [31]. As anticipated, similar treatment trends to those observed in acute OM were noted (Fig. 4b). Rats treated with 1%FRS and FRS-OFL exhibited no evident suppuration in the TM on days 42 and 56, indicating lower infection rates in the FRS groups. In contrast, rats in the non-FRS CON and OFL-treated groups displayed yellowing of the TM, along with severe hypertrophic scarring and purulent inflammation. Notably, in the CSOM model, we observed spontaneous polymicrobial infections (Fig. 4b). On day 14 of FRS treatment, the bacterial culture results from the middle ear revealed the presence of various colonies in all treatment groups. In the untreated control group, the predominant colonies were those of *P. aeruginosa* (used in the model, appearing as flat green colonies) with a few *S. aureus* colonies (appearing as small white dots). In the FRS-OFL treatment group, *S. aureus* was predominant, with a few *P. aeruginosa* colonies present. However, in the OFL and 1% FRS groups, no *P. aeruginosa* colonies were observed, and the number of *S. aureus* colonies was significantly reduced. This indicates that during the course of chronic otitis media, the rats experienced secondary bacterial infections. In untreated rats, both the primary infection was severe and persistent, and the secondary infections were relatively serious. In contrast, 1% FRS effectively limited the primary bacterial infection, protecting the middle ear tissue and significantly reducing the severity of secondary bacterial infections. Consequently, the disease severity scores of 1%FRS (2.8±0.8) and FRS-OFL (3.4±0.5)

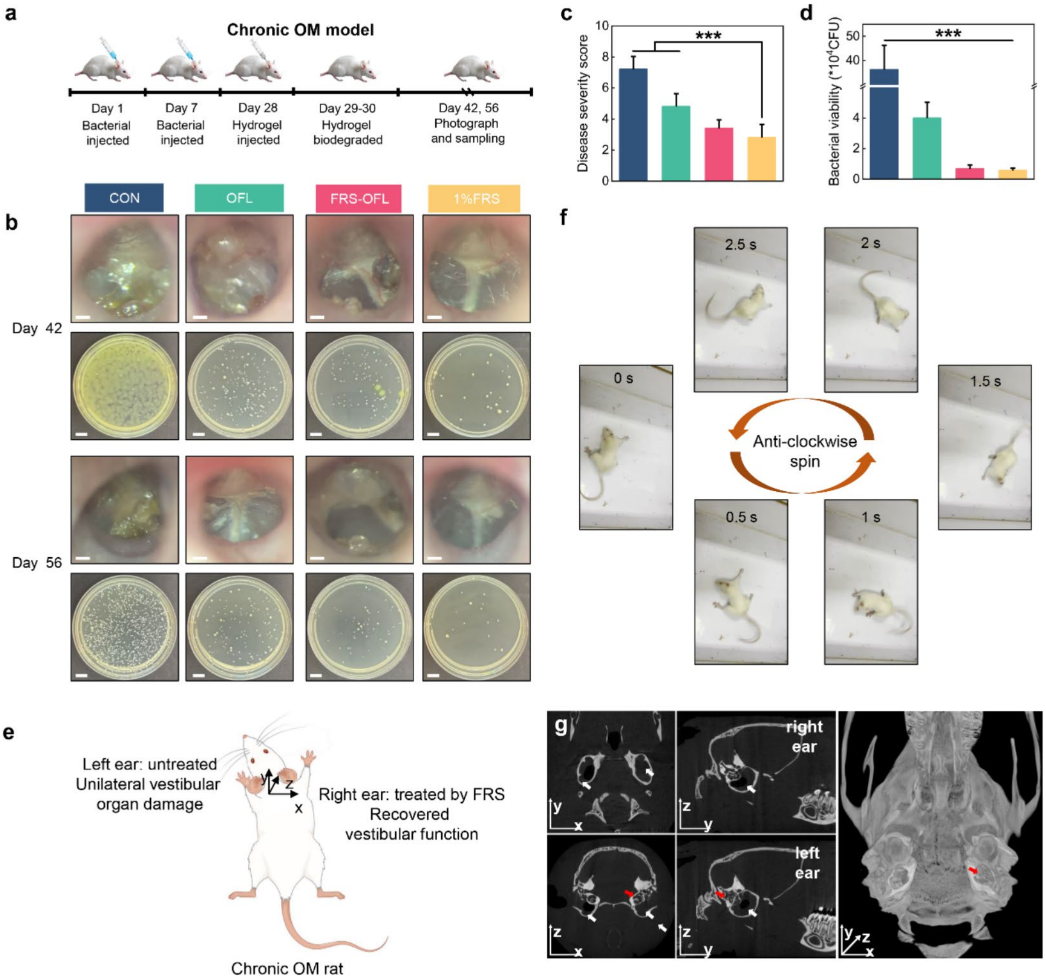

Fig. 4 Optimum therapeutic efficacy of 1%FRS on chronic OM rat. (**a**) Schematic representation showing the procedure of the establishment and treatment of chronic OM rat. (**b**) Representative images of the infected TMs and residual bacteria in ME on day 42 and 56 after treated by CON, OFL, FRS-OFL and 1%FRS. (**c**) The estimated disease severity score of healed TMs and (**d**) calculated residual bacteria viability in ear of different groups. (**e**) Schematic diagram of the chronic OM rat with left ear untreated and right ear treated with 1%FRS, resulting in asymmetric vestibular dysfunction. (**f**) A set of photos showing the anti-clockwise spin of above chronic OM rat in seconds. (**g**) Micro-CT images showing the 3D reconstructions of the chronic OM rat brain with recovered right ear and damaged left ear at day 56. All statistical analyses were performed by one-way ANOVA, data represent mean ± standard deviation, $^{***}p < 0.001$

were notably lower than those of CON (7.2±0.8) and OFL (4.8±0.8), as were the residual bacterial viabilities (0.56±0.15 $*10^4$ CFU for 1%FRS, 0.67±0.25 $*10^4$ CFU for FRS-OFL, 36.19±9.98 $*10^4$ CFU for CON, 3.99±1.04 $*10^4$ CFU for OFL), shown in Fig. 4c and d. It is important to highlight that the therapeutic efficacy of 1%FRS surpassed that of the clinically used OFL, underscoring the significant potential of FRS hydrogels in the clinical management of OM.

The vestibular function of the treated rats was evaluated, as prolonged and recurrent infections in chronic OM rats not only led to ME inflammation but also resulted in vestibular function impairment, causing balance issues in the rats. As depicted in Fig. 4e, to visually demonstrate the therapeutic benefits of FRS hydrogels in chronic OM, we treated the right ear of a chronic OM rat with 1%FRS, leaving the left ear untreated as a control. Intriguingly, behavioral analysis revealed that this chronic OM rat exhibited anti-clockwise spinning in the absence of external stimuli (Fig. 4f), indicating severe unilateral vestibular organ damage in the untreated left ear and restored vestibular function in the right ear (see Movie S1). Additionally, to assess the severity of lesions in the ME, micro-computed tomography (micro-CT) scans were performed on normal rats and chronic OM rats. The results in Fig. S9 demonstrated that the temporal cavity of normal rats appeared hollow, whereas hypodense shadows (indicated by white arrows) were observed in the temporal cavity of chronic OM rats, suggesting the presence of residual fluid accumulation. Furthermore, as shown in Fig. 4g, the affected left ear of the chronic OM rat with vestibular dysfunction exhibited substantial fluid accumulation (white arrow) and noticeable structural damage to the inner ear (red arrow), while the contralateral right ears treated with 1%FRS remained structurally intact. The micro-CT and behavioral findings corroborated that 1%FRS effectively impeded the progression and deterioration of chronic OM to a certain extent, preventing further damage.

ABR test of FRS-treated OM rats

To assess the hearing recovery and biocompatibility of FRS in the ear, we conducted auditory brainstem response (ABR) tests to evaluate the hearing of FRS-treated rats. ABR is a type of electroencephalogram signal that responds to auditory stimuli and is commonly used to assess potential auditory function disorders within the brain. The experimental setup is illustrated in Fig. 5a, where rats were positioned in an anechoic chamber to eliminate electromagnetic and acoustic interference during the experiments. Further details on the experimental procedure and setup can be found in the Supporting Information. Representative waveforms of an untreated OM rat, an OM rat treated with FRS, and a healthy rat in response to clicks (100 µs duration) are depicted in Fig. 5b, with the black lines denoting the specific sound pressure level (SPL) of the acoustic stimulation, revealing discernible peaks characteristic of regular III and V responses. The corresponding calculated ABR thresholds are presented in Fig. 5c and S10, where the threshold of FRS-treated rats, particularly the 1%FRS group, was significantly lower than that of untreated OM rats for both click and all pure tone stimuli (1, 2, 4, 8, 16, and 32 kHz) on day 14. Notably, no statistical difference in ABR thresholds was observed between normal rats and those treated with FRS, indicating successful hearing recovery in FRS-treated rats.

To further elucidate the improvement in hearing, we analyzed ABR wave I amplitudes, reflecting the number of firing neurons, and ABR wave I latencies, indicating the speed of transmission. At day 7, FRS-treated rats exhibited significantly higher ABR wave I amplitudes at frequencies of 4, 8, and 16 kHz compared to untreated OM rats (Fig. 5d). Moreover, the amplitude of the representative waveform of FRS-treated OM rat evoked by click was notably higher than that of untreated OM rat (Fig. 5e). Similarly, shorter ABR wave I latencies in FRS-treated rats compared to untreated OM rats suggested a reduced delay in cochlear nerve transmission (Fig. 5f) [32]. In Fig. S10b, the waveforms of untreated and FRS-treated OM rats displayed higher amplitudes and lower latencies in the FRS group, indicating improved hearing. Collectively, these findings demonstrate an enhancement in hearing in FRS-treated OM rats.

To assess whether the hearing has returned to normal, a comparison of ABR results between healthy rats and FRS-treated rats is presented in Fig. 5g and h. The ABR threshold of 1%FRS-treated rats was nearly equivalent to that of healthy rats after 14 days, although differences in wave amplitude and latency persisted. However, by day 28, the hearing data were nearly identical, indicating complete restoration of hearing in 1%FRS-treated rats. These results suggest that FRS is non-ototoxic, providing an additional advantage over antibiotics.

The cytocompatibility of FRS hydrogels was evaluated in Fig. S11 through live/dead assays of mouse fibroblast L929 cells, primarily utilizing 2%FRS due to its higher content. As depicted in Fig. S11a-c, no significant differences in viable cells were observed between the CON and FRS groups after a 24-hour incubation period, indicating that FRS hydrogels did not impact cell growth and proliferation. Regarding the potential long-term risks associated with FRS, previous clinical studies have demonstrated the safety of CS as an oral medication in humans [44]. Therefore, we further investigated whether FRS has any adverse effects on the structure of middle ear tissues, we performed micro-CT scans on rats two months after FRS treatment (Fig. 4g, S9). The results

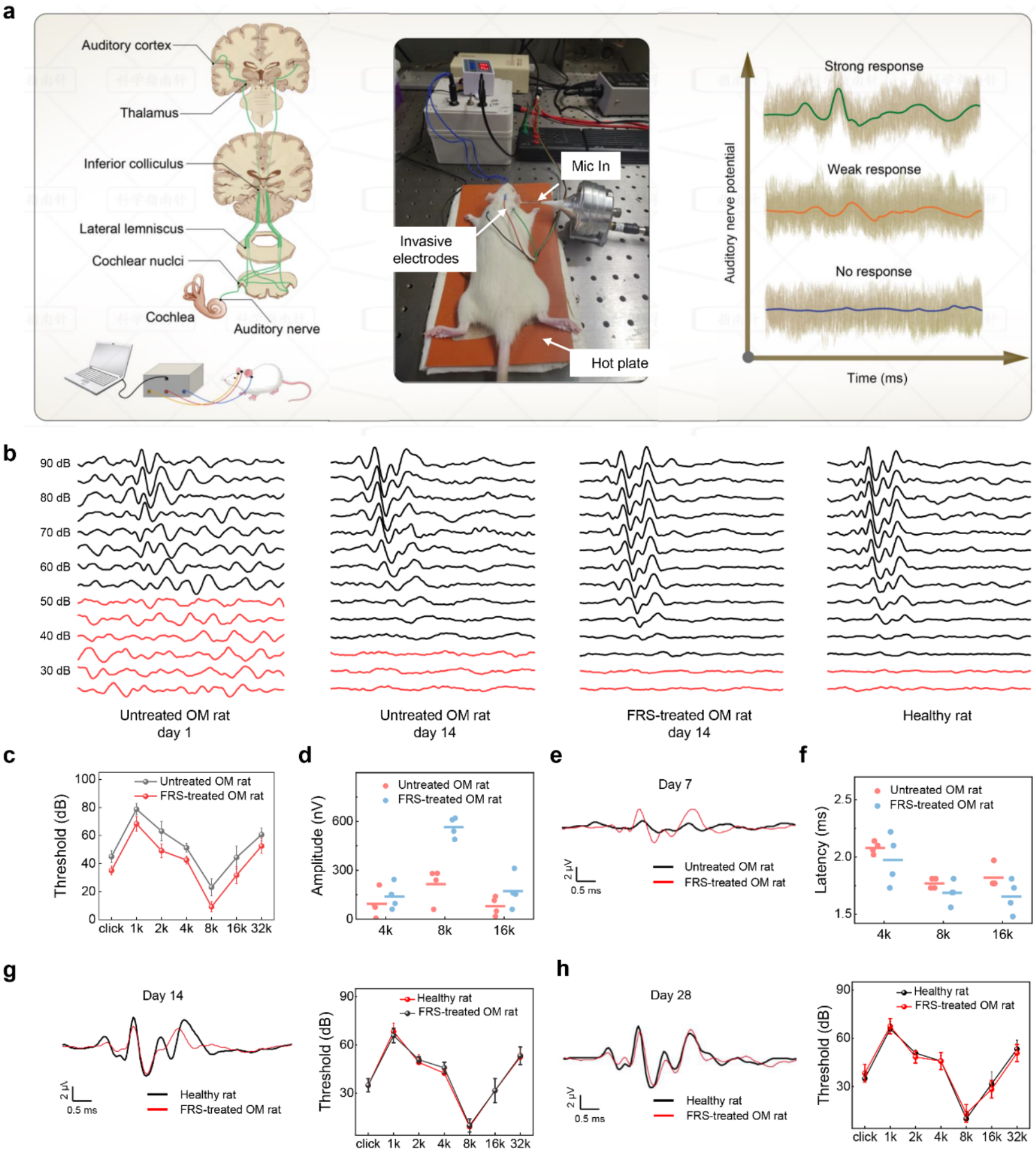

Fig. 5 Auditory brainstem response (ABR) test of the FRS treated rats. (**a**) Schematic representation of neurons in the auditory nerve and brainstem firing in response to evoked acoustic stimulus activity, and photos of the ABR experimental set-up. (**b**) Representative ABR waveforms evoked by click of different rats under acoustic stimulation. (**c**) The calculated ABR threshold of untreated and 1%FRS treated rats at day 14 under different frequencies stimulation. (**d**) The measured ABR wave I amplitude of untreated and 1%FRS treated rats. (**e**) ABR waveform evoked by click of untreated and 1%FRS treated rats at day 7, and (**f**) their measured latency. (**g**, **h**) Comparison of ABR waveforms evoked by click and their threshold of healthy and 1%FRS treated rats at day 14 and day 28, showing the hearing recovery of FRS treated rats

demonstrated that the middle ear structure of the treated ears remained intact and healthy. To assess the potential allergic risk associated with FRS, we conducted RNA-seq analysis on middle ear tissues from rats treated with FRS (Fig S11d). The results showed no statistically significant differences in the expression of genes related to allergic reactions compared to the control group, indicating a low risk of allergic responses induced by FRS. Furthermore, to assess biocompatibility in vivo, as shown in Fig. S11e, rats injected with 2%FRS for 7 days were euthanized to obtain tissue samples from major organs (heart, liver, spleen, lung, and kidney). Histopathological examinations from H&E staining sections revealed no significant pathological damage induced by FRS injection in the major organs, indicating the absence of organ toxicity associated with FRS treatment.

Bacteriostatic activity of FRS hydrogels against multiple pathogenic bacterial of OM

Broad-spectrum antibacterial properties are crucial for the effective treatment of OM due to the presence of diverse pathogenic bacteria. In addition to the antibiotic-resistant *S. aureus* demonstrated in Fig. 2, we investigated the broad-spectrum antibacterial and antibiofilm capabilities of FRS against Gram-positive bacteria *S. aureus*, *S. pneumoniae*, and Gram-negative bacteria *P. aeruginosa* and *E. coli*. As depicted in Fig. 6a, live bacterial images were captured after 6 h of incubation, followed by direct live/dead staining or dilution and an additional 24 h of incubation. Hydrogels with a gradient of CS concentration were utilized to illustrate that the primary antimicrobial activity in FRS stemmed from

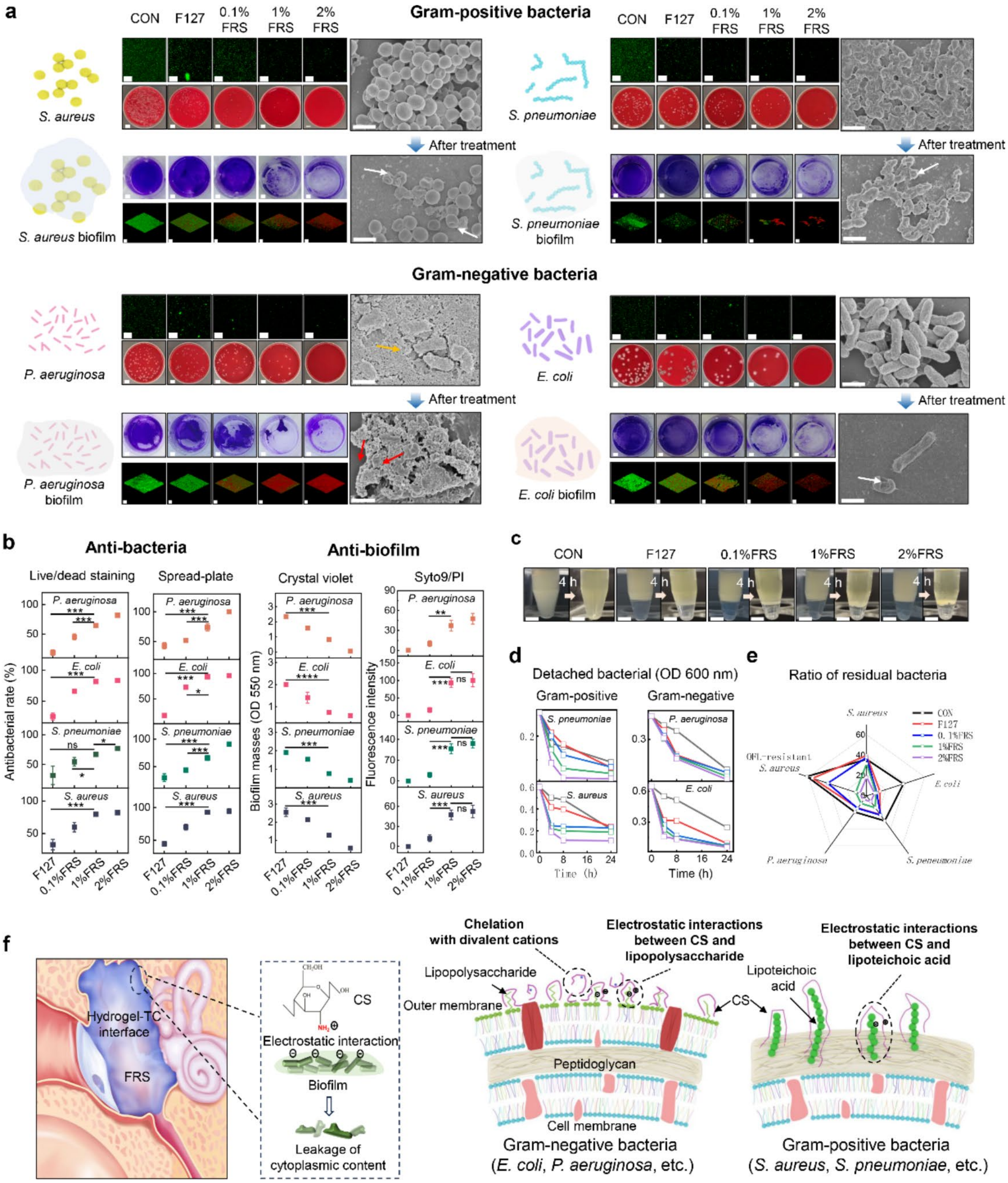

Fig. 6 Antibacterial and antibiofilm properties of FRS hydrogels in vitro. (**a**) Fluorescence staining (scale bar: 100 μm) and spread-plate culture photos (scale bar: 1 cm) of common clinical OM pathogenic bacterial treated by different groups, including Gram-positive *S. aureus*, *S. pneumoniae*, and Gram-negative *P. aeruginosa*, *E. coli*. The color of the *S. pneumoniae* colonies is similar to that of the blood agar plate. To facilitate identification, we have circled the colonies in white on the images. Photos of biofilms stained with Crystal violet (scale bar: 2 mm), or Syto-9/PI (scale bar: 100 μm). Representative SEM images of treated bacterial with shrunk morphologies (scale bar: 1 μm). (**b**) The corresponding statistical data of different groups against multiple OM pathogenic bacterial and biofilms, including F127 and FRS with different content of CS. (**c**-**e**) The calculated detached bacterial and ratio of residual bacteria of different treatment groups through bacteria aggregation process (scale bar: 5 mm). All statistical analyses were performed by one-way ANOVA, data represent mean ± standard deviation, ns > 0.05, *$p < 0.05$, **$p < 0.01$, ***$p < 0.001$

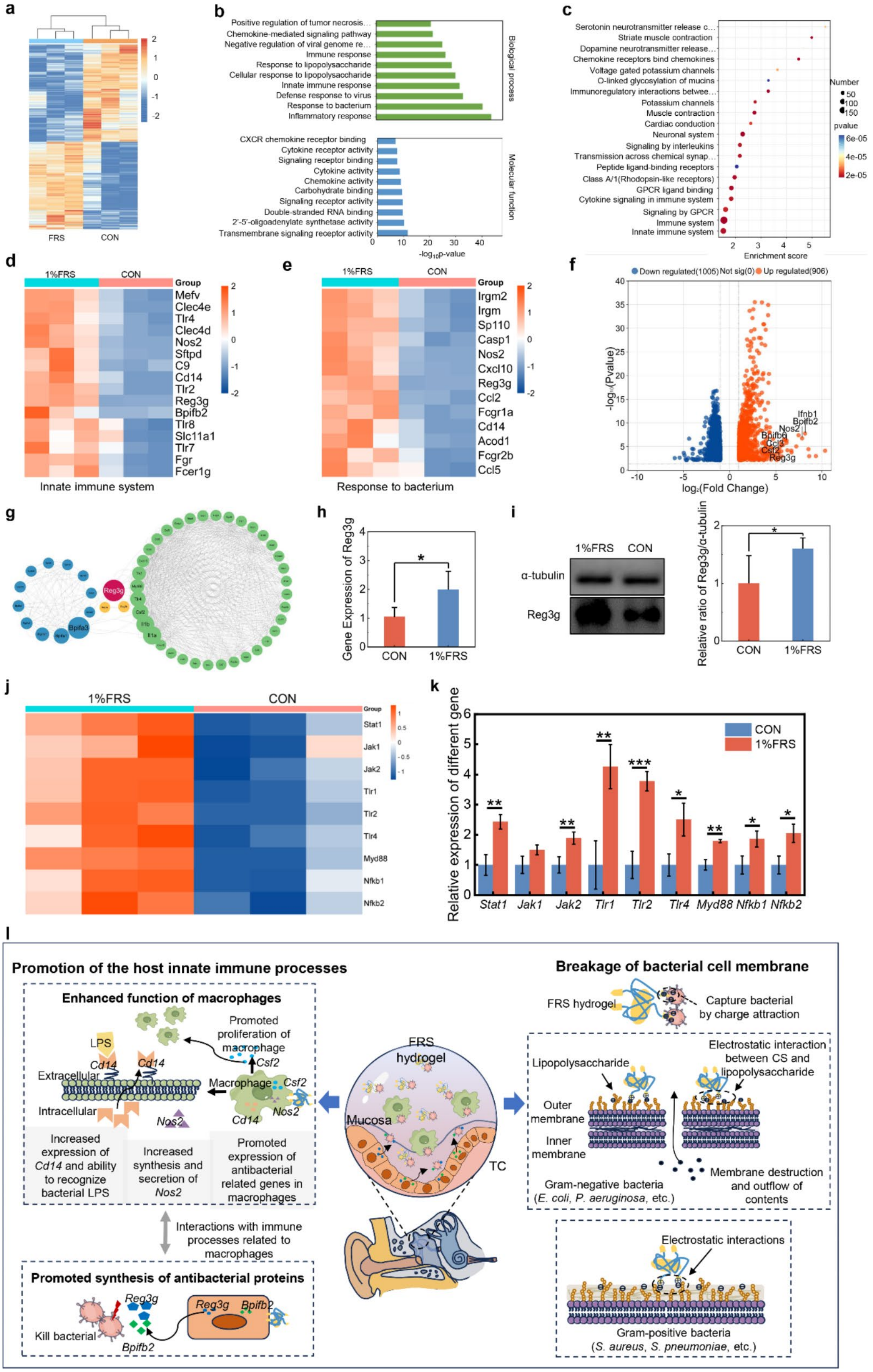

Fig. 7 (See legend on next page.)

(See figure on previous page.)

Fig. 7 FRS enhances the therapeutic effect of OM by promoting innate immune processes. (**a**) Heat maps of the differential gene expression (**b**) GO functional enrichment analysis of DEGs between the CON and 1%FRS groups. (**c**) Reactome enrichment analysis of differential gene. (**d**) Reactome enrichment analysis of differential gene. (**e**) Heat map summarizing the associated enriched GO terms. (**f**) Volcano plot of differential gene expression. (**g**) Protein-protein interaction network analysis of the enriched gene. (**h**) RT-qPCR analysis of *Reg3g* expression of CON group and 1%FRS group. (**i**) Representative immunoblot of rat ear bullae from CON and 1%FRS group, with detection of *Reg3g* and *α-tubulin* as loading control; And the relative ratio of them quantified by densitometry. (**j**) The activation of pathways involved in the enhanced innate immunity induced by FRS. (**k**) RNA sequencing results of gene expression during the interaction between FRS and the immune system (**l**) Schematic illustration of the potential mechanisms of FRS for treating OM. All statistical analyses were performed by one-way ANOVA, data represent mean ± standard deviation, $^*p < 0.05$

CS, with antibacterial rates calculated through live/dead staining and spread plate methods. Increasing CS concentration led to a reduction in the remaining viable bacteria stained green and their cultured colonies on blood agar plates. SEM images showcased significant alterations in the morphology of the cultured bacteria post-incubation with FRS, with evident collapse in surface structure. Particularly, SEM images of *P. aeruginosa* highlighted clear disruption of dense biofilms by FRS treatment. Additionally, in blood agar plates simultaneously inoculated with the four aforementioned bacteria, FRS maintained strong antibacterial activity, demonstrating its effectiveness in combating multiple bacterial infections simultaneously (Fig. S13). This suggests that FRS has the potential to better address complex clinical infection scenarios. We also compared the inhibition zones of FRS and OFL against these bacteria (Fig S12). Although the aqueous solution of ofloxacin exhibited slightly larger inhibition zones due to its superior diffusion capability, FRS effectively killed bacteria in the areas where it made contact with the bacterial culture plates. Therefore, in the more anatomically complex middle ear, we can still anticipate that FRS will exhibit antibacterial effects comparable to those of OFL, as demonstrated in the aforementioned animal experiments (Figs. 2, 3, 4 and 5).

Given that 1%FRS exhibited optimal therapeutic efficacy for OM in vivo, our focus was on detailing the antibacterial efficiency of 1%FRS. Statistically, as shown in Fig. 6b, the antibacterial rates of 1%FRS against *S. aureus*, *S. pneumoniae*, *E. coli*, and *P. aeruginosa* were 92.73% ± 2.02%, 65.71% ± 4.67%, 93.62% ± 0.05%, and 73.56% ± 6.17%, respectively. Furthermore, we assessed FRS's ability to disrupt biofilms of various pathogens through crystal violet staining and Syto9/PI staining. Crystal violet staining revealed that biofilms in the CON, F127, and 0.1%FRS groups remained largely viable and structurally intact, whereas with increasing CS concentration, 1%FRS and 2%FRS effectively disrupted the biofilms of common OM pathogens, leading to substantial biomass loss. Three-dimensional reconstructions of live/dead staining of these bacterial biofilms using CLSM indicated increased dead bacteria in the 1%FRS and 2%FRS groups. Notably, the linear variation in biofilm loss rate of the four OM pathogens as a function of CS content became more pronounced, with the optical density (OD550) values of 1%FRS (1.29±0.08 of *S. aureus*, 0.78±0.05 of *S. pneumoniae*, 0.75±0.03 of *E. coli*, 0.83±0.06 of *P. aeruginosa*) approximately 2–4 times lower than those of the CON group (2.76±0.13 of *S. aureus*, 2.29±0.03 of *S. pneumoniae*, 2.47±0.03 of *E. coli*, 2.83±0.11 of *P. aeruginosa*), demonstrating that FRS possessed excellent broad-spectrum antibacterial properties and remarkable inhibition effect on OM pathogens biofilm formation.

The aggregation was characterized in Fig. 6c, after 24-hour incubation and 4-hour free settling, the upper bacterial fluid showed different absorbances, shown in Fig. 6d. As the concentration of CS increased, the adsorption capacity of the hydrogels to multiple OM pathogens increased. After conversion, as shown in Fig. S14 and 6e, the ratio of residual bacteria in 1%FRS solution at 24 h (31.67% of *S. aureus*, 14.33% of *S. pneumoniae*, 9.69% of *E. coli*, 9.30% of *P. aeruginosa*), significantly lower than those of CON (35.89% of *S. aureus*, 30.33% of *S. pneumoniae*, 38.05% of *E. coli*, 19.68% of *P. aeruginosa*) and F127 (39.61% of *S. aureus*, 22.67% of *S. pneumoniae*, 13.85% of *E. coli*, 14.71% of *P. aeruginosa*), demonstrating the excellent adsorption capacity of 1%FRS against multiple OM pathogens.

Promotion of host's innate immunity by FRS to combat bacterial invasion

To elucidate the potential molecular mechanisms underlying the excellent efficacy of composite gel therapy for OM in rats, RNA sequencing (RNA-seq) analysis was conducted on extracted ME pouches. The results revealed robust correlation among the test samples (Fig. 7a), with 1911 differentially expressed genes identified between the 1%FRS-treated group, including 906 downregulated and 1005 upregulated genes (Fig. S15). Gene Ontology (GO) enrichment analysis of these differentially expressed genes indicated significant modulation of crucial biological processes in response to bacterial infection, including inflammation response (GO:0006954), response to bacteria (GO:0009617), innate immunity (GO:0045087), and cellular response to lipopolysaccharide (GO:0071222). Moreover, molecular functional processes like cytokine (GO:0005125) and chemokine activity (GO:0008009) (Fig. 7b) were notably regulated. These findings suggest that 1%FRS not only possesses bactericidal properties but may also enhance the host defense against bacteria by modulating the immune response.

Furthermore, we performed enrichment analysis using the Reactome database. The results demonstrated significant regulation by the composite gel in experimental groups of biological processes such as the innate immune system, immune system (R-RNO-168256), adaptive immune system (R-RNO-1280218), and cytokine signaling in the immune system (R-RNO-1280215) (Fig. 7c).

Integrating the results from both databases, we identified genes that may play essential roles in combating bacterial invasion and facilitating disease recovery. Notably, genes directly involved in antimicrobial functions (Fig. 7d), such as *Reg3g*, *Bpifb2*, *Bpifb6*, *Sp110*, and *Ifnb1*, were observed. Genes regulating inflammation response, including *Acod1*, which prevents excessive inflammation and reduces tissue damage, were identified. Intriguingly, a substantial number of genes associated with macrophages were found among the enriched genes (Fig. 7e), such as macrophage colony-stimulating factor *Csf2*, chemotactic factors *Ccl2* and *Ccl7*, and *Nos2*, which mediates macrophage bactericidal activity. Hence, we speculate that FRS can rapidly activate the host's innate immune system, enabling a swifter response to bacterial intrusion.

To further elucidate the antibacterial mechanism, we focused on genes with significantly higher fold changes and upregulation, such as *Reg3g*, *Csf2*, and *Bpifb2* (Fig. 7f). Protein-protein interaction network analysis of the proteins translated from these genes revealed that the antimicrobial peptide *Reg3g* played a crucial role (Fig. 7g). Besides its own mucosal immune function, *Reg3g* also regulated the expression of bactericidal/permeability-increasing protein-like family proteins and modulated macrophage activity. Consequently, through RT-qPCR and western-blot (WB) results, it was experimentally demonstrated that the relative expression levels of the *Reg3g* gene (Fig. 7h) and the expression levels of the antimicrobial peptide *Reg3g* (Fig. 7i) were significantly increased. At this point, we proceeded to further investigate the interaction between the hydrogel and host tissues. According to previous studies [45], chitosan can promote macrophage polarization towards the M1 phenotype, a process that involves the activation of the JAK/STAT1 pathway (Fig. 7j and k) [46]. M1 macrophages, characterized by high expression of Nos2, play a crucial role in the early response to bacterial infections by secreting cytokines such as IFN-γ, CSF2, and IL-23. IFN-γ further promotes M1 macrophage polarization, while IL-23 enhances IL-22 expression, which subsequently stimulates the production of antimicrobial proteins like REG3G through the activation of the STAT3 pathway [47]. Moreover, M1 macrophages express Toll-like receptors (TLRs), which recognize bacterial components during infection and activate the TLR/MyD88/NF-κB pathway to promote the release of inflammatory cytokines that combat bacterial infections (Fig. 7j and k). To verify the expression of these cytokines and the activation of signaling pathways, we analyzed the RNA-seq results during the early stages of infection. As shown in Fig S16, compared to the untreated control group, the expression levels of M1 macrophage markers in the 1% FRS treatment group were significantly increased, indicating enhanced M1 macrophage polarization. Additionally, the pathways involved in macrophage polarization and the antibacterial response, including JAK/STAT and TLR/MyD88/NF-κB, were notably activated. Therefore, we propose that FRS, through its chitosan component, interacts with macrophages to promote M1 polarization, thereby enhancing the innate immune response in the early stages of infection. This, in turn, increases resistance to bacterial invasion, shortens the infection duration, and accelerates the overall recovery process.

Overall, we have found that the excellent therapeutic effect of FRS on OM is attributed to two routes. (1) FRS realizes the bactericidal activity by disrupting bacterial cell membranes through electrostatic interactions or non-covalent binding with membrane constituents, thereby disrupting the normal physiological function of the bacterial cell membrane and causing bacterial death. (2) FRS enhances the host's innate immune response against bacteria by promoting the synthesis of antimicrobial proteins such as *Reg3g* and bactericidal/permeability-increasing protein-like family proteins, as well as the proliferation and functional activation of macrophages, thus bolstering the host's defense against bacteria. Thus, FRS not only exhibits significant bactericidal capability but also augments the host's defense mechanisms against bacteria, thereby achieving favorable therapeutic outcomes (Fig. 7j, l).

Conclusion

In conclusion, previous researchers have developed new treatment strategies, including the use of chemical permeation enhancers to improve drug permeability through the tympanic membrane, as well as the use of bacteriophages and metal ion compounds. However, these approaches often fall short in terms of cost control and biocompatibility. Therefore, the droppable, conformal, and immunomodulatory FRS hydrogels exhibit exceptional broad-spectrum antibacterial properties, making them a promising treatment option for OM. The study encompassed the design and characterization of the hydrogel, highlighting favorable physicochemical attributes such as injectability, conformal contact, biodegradability, and biocompatibility. Through a series of in vitro and in vivo experiments, the hydrogel demonstrated potent antibacterial effects against common pathogens and antibiotic-resistant strains associated with OM, effectively eradicating biofilms to prevent chronic conditions and reduce the risk of hearing loss and complications. Additionally, the molecular mechanisms underlying FRS's efficacy in modulating the immune response were elucidated, showcasing its potential to enhance antimicrobial protein synthesis and macrophage-related gene expression. Moreover, FRS hydrogels have the potential to carry other components, such as anti-inflammatory drugs, and their metabolic rate can be adjusted. These aspects will be further explored in our future work to better serve clinical treatment processes. Overall, the FRS hydrogel presents a promising, cost-effective, and convenient therapeutic approach for OM, benefiting patient care and future research in the field.

Supplementary Information

The online version contains supplementary material available at https://doi.org/10.1186/s12951-024-02908-4.

Supplementary Material 1

Supplementary Material 2

Acknowledgements
Not applicable.

Author contributions
Y.J. and Y.S. contributed equally to this work. H.W., L.L. and S.Y. designed and directed the project. Y.J., Y.S. and C.W. performed the experiments. Z.C. and H.S. supervised the experiments and edited the paper. Y.J., H.W., L.L. and S.Y. wrote the manuscript with the revisions of all authors.

Funding
This study was financially supported by National Natural Science Foundation of China (82301331, 82330034, 82271161, 82071041), Shanghai Pujiang Program (22PJD050), Interdisciplinary Program of Shanghai Jiao Tong University (YG2023LC11), Shanghai Municipal Commission of Science and Technology (18DZ2260200), Shanghai Top-Priority Research Center Project (2023ZZ02008).

Data availability
No datasets were generated or analysed during the current study.

Declarations

Ethics approval and consent to participate
This study was approved by the Animal Welfare Ethics Committee of Shanghai Sixth People's Hospital Affiliated with Shanghai Jiao Tong University, School of Medicine (No. DWLL2024-0557).

Consent for publication
All authors agree to be published.

Competing interests
The authors declare no competing interests.

Received: 22 July 2024 / Accepted: 5 October 2024

References

1. Schilder AG, Chonmaitree T, Cripps AW, Rosenfeld RM, Casselbrant ML, Haggard MP. RP Venekamp. Otitis media. Nat Rev Dis Primers. 2016;2:16063.
2. Monasta L, Ronfani L, Marchetti F, Montico M, Vecchi Brumatti L, Bavcar A, Grasso D, Barbiero C, Tamburlini G. Burden of disease caused by otitis media: systematic review and global estimates. PLoS ONE. 2012;7:e36226.
3. Browning GG, Weir J, Kelly G, Swan IRC. Chronic otitis media. CRC; 2018. pp. 977–1019.
4. Rizk HG, Lee JA, Liu YF, Endriukaitis L, Isaac JL, Bullington WM. Drug-Induced ototoxicity: a Comprehensive Review and Reference Guide. Pharmacotherapy. 2020;40:1265–75.
5. Selimoglu E. Aminoglycoside-induced ototoxicity. Curr Pharm Des. 2007;13:119–26.
6. Ray P, Singh S, Gupta S. Topical antimicrobial therapy: current status and challenges. Indian J Med Microbiol. 2019;37:299–308.
7. Argaw-Denboba A, Abejew AA, Mekonnen AG. Antibiotic-resistant Bacteria are major threats of Otitis Media in Wollo Area, northeastern Ethiopia: a ten-year retrospective analysis. Int J Microbiol. 2016;2016:8724671.
8. Nguyen TN, Park J-S. Intratympanic drug delivery systems to treat inner ear impairments. J Pharm Investig. 2022;53:93–118.
9. Gupta A, Mumtaz S, Li CH, Hussain I, Rotello VM. Combatting antibiotic-resistant bacteria using nanomaterials. Chem Soc Rev. 2019;48:415–27.
10. Sun A, He X, Li L, Li T, Liu Q, Zhou X, Ji X, Li W, Qian Z. An injectable photopolymerized hydrogel with antimicrobial and biocompatible properties for infected skin regeneration. NPG Asia Mater. 2020;12.
11. Fjell CD, Hiss JA, Hancock RE, Schneider G. Designing antimicrobial peptides: form follows function. Nat Rev Drug Discov. 2011;11:37–51.
12. Modi SK, Gaur S, Sengupta M, Singh MS. Mechanistic insights into nanoparticle surface-bacterial membrane interactions in overcoming antibiotic resistance. Front Microbiol. 2023;14:1135579.
13. Tang S, Zheng J. Antibacterial activity of silver nanoparticles: Structural effects. Adv Healthc Mater. 2018;7:e1701503.
14. Zhou L, Zheng H, Liu Z, Wang S, Liu Z, Chen F, Zhang H, Kong J, Zhou F, Zhang Q. Conductive antibacterial hemostatic multifunctional scaffolds based on Ti(3)C(2)T(x) MXene nanosheets for promoting Multidrug-resistant Bacteria-infected Wound Healing. ACS Nano. 2021;15:2468–80.
15. Lu X, Feng X, Werber JR, Chu C, Zucker I, Kim JH, Osuji CO, Elimelech M. Enhanced antibacterial activity through the controlled alignment of graphene oxide nanosheets. Proc Natl Acad Sci U S A. 2017;114:E9793–801.
16. Qi M, Wang X, Chen J, Liu Y, Liu Y, Jia J, Li L, Yue T, Gao L, Yan B, et al. Transformation, absorption and Toxicological Mechanisms of Silver Nanoparticles in the gastrointestinal tract following oral exposure. ACS Nano. 2023;17:8851–65.
17. Indumathi MP, Saral Sarojini K, Rajarajeswari GR. Antimicrobial and biodegradable chitosan/cellulose acetate phthalate/ZnO nano composite films with optimal oxygen permeability and hydrophobicity for extending the shelf life of black grape fruits. Int J Biol Macromol. 2019;132:1112–20.
18. Wang H, Gong X, Miao Y, Guo X, Liu C, Fan YY, Zhang J, Niu B, Li W. Preparation and characterization of multilayer films composed of chitosan, sodium alginate and carboxymethyl chitosan-ZnO nanoparticles. Food Chem. 2019;283:397–403.
19. Shah A, Yameen MA, Fatima N, Murtaza G. Chemical synthesis of chitosan/silver nanocomposites films loaded with moxifloxacin: their characterization and potential antibacterial activity. Int J Pharm. 2019;561:19–34.
20. Dongol K, Rayamajhi P, Gurung U. Complications of Acute and Chronic Otitis Media in a Tertiary Referral Center in Nepal. Turk Arch Otorhinolaryngol. 2020;58:234–40.
21. Chen H, Zhang H, Dai Y, Zhu H, Hong G, Zhu C, Qian X, Chai R, Gao X, Zhao Y. Magnetic hydrogel Microrobots Delivery System for Deafness Prevention. Adv Funct Mater. 2023;33.
22. Kono M, Umar NK, Takeda S, Ohtani M, Murakami D, Sakatani H, Kaneko F, Nanushaj D, Hotomi M. Novel Antimicrobial Treatment Strategy based on drug Delivery systems for Acute Otitis Media. Front Pharmacol. 2021;12:640514.
23. Dahroug B, Tamadazte B, Weber S, Tavernier L, Andreff N. Review on Otological Robotic Systems: toward Microrobot-assisted cholesteatoma surgery. IEEE Rev Biomed Eng. 2018;11:125–42.
24. Ahmad A, Ullah S, Ahmad W, Yuan Q, Taj R, Khan AU, Rahman AU, Khan UA. Zinc oxide–selenium heterojunction composite: synthesis, characterization and photo-induced antibacterial activity under visible light irradiation. J Photochem Photobiol B. 2020;203:111743.
25. Kumari N, Kumar S, Karmacharya M, Dubbu S, Kwon T, Singh V, Chae KH, Kumar A, Cho YK, Lee IS. Surface-textured mixed-metal-oxide nanocrystals as efficient catalysts for ROS Production and Biofilm Eradication. Nano Lett. 2021;21:279–87.
26. Debnath S, Shome A, Das D, Das PK. Hydrogelation through self-assembly of fmoc-peptide functionalized cationic amphiphiles: potent antibacterial agent. J Phys Chem B. 2010;114:4407–15.

27. Qi R, Zhang N, Zhang P, Zhao H, Liu J, Cui J, Xiang J, Han Y, Wang S, Wang Y. Gemini peptide amphiphiles with Broad-Spectrum Antimicrobial Activity and Potent Antibiofilm Capacity. ACS Appl Mater Interfaces. 2020;12:17220–29.
28. Li S, Gu B, Li X, Tang S, Zheng L, Ruiz-Hitzky E, Sun Z, Xu C, Wang X. MXene-Enhanced chitin composite sponges with antibacterial and hemostatic activity for Wound Healing. Adv Healthc Mater. 2022;11:e2102367.
29. Cao J, Zhang T, Zhu W, Li HB, Shen AG. A cooling-driven self-adaptive and removable hydrogel coupled with combined chemo-photothermal sterilization for promoting infected wound healing. Nanoscale. 2023;15:11163–78.
30. Ko YS, Gi EJ, Lee S, Cho HH. Dual red and near-infrared light-emitting diode irradiation ameliorates LPS-induced otitis media in a rat model. Front Bioeng Biotechnol. 2023;11:1099574.
31. Ersoy Callioglu E, Bercin S, Basdemir G, Kiris M, Tatar I, Tuzuner A, Oguzhan T, Muderris T, Sargon MF, Korkmaz MH. The effect of N-acetyl cysteine on biofilm layers in an experimental model of chronic otitis media. Acta Otorhinolaryngol Ital. 2020;40:457–62.
32. Milloy V, Fournier P, Benoit D, Norena A, Koravand A. Auditory brainstem responses in Tinnitus: a review of who, how, and what? Front Aging Neurosci. 2017;9:237.
33. Packirisamy RG, Govindasamy C, Sanmugam A, Karuppasamy K, Kim HS. D Vikraman. Synthesis and Antibacterial properties of Novel ZnMn(2)O(4)-Chitosan nanocomposites. Nanomaterials. (Basel). 2019;9(11):1589.
34. Motshekga SC, Ray SS, Onyango MS, Momba MNB. Preparation and antibacterial activity of Chitosan-based nanocomposites containing bentonite-supported silver and zinc oxide nanoparticles for water disinfection. Appl Clay Sci. 2015;114:330–39.
35. Han H, Yang J, Li X, Qi Y, Yang Z, Han Z, Jiang Y, Stenzel M, Li H, Yin Y, et al. Shining light on transition metal sulfides: new choices as highly efficient antibacterial agents. Nano Res. 2021;14:2512–34.
36. Gan BH, Siriwardena TN, Javor S, Darbre T, Reymond JL. Fluorescence imaging of bacterial killing by antimicrobial peptide dendrimer G3KL. ACS Infect Dis. 2019;5:2164–73.
37. Ye R, Xu H, Wan C, Peng S, Wang L, Xu H, Aguilar ZP, Xiong Y, Zeng Z, Wei H. Antibacterial activity and mechanism of action of epsilon-poly-L-lysine. Biochem Biophys Res Commun. 2013;439:148–53.
38. Wang X, Qi J, Zhang W, Pu Y, Yang R, Wang P, Liu S, Tan X. Chi. 3D-printed antioxidant antibacterial carboxymethyl cellulose/epsilon-polylysine hydrogel promoted skin wound repair. Int J Biol Macromol. 2021;187:91–104.
39. Liu L, Xiong S, Zeng L, Cai C, Li F, Tan Z. Two birds with one stone: porous poly(ionic liquids) membrane with high efficiency for the separation of amino acids mixture and its antibacterial properties. J Colloid Interface Sci. 2021;584:866–74.
40. Mei L, Zhu S, Yin W, Chen C, Nie G, Gu Z, Zhao Y. Two-dimensional nanomaterials beyond graphene for antibacterial applications: current progress and future perspectives. Theranostics. 2020;10:757–81.
41. Li Y, Wang D, Wen J, Yu P, Liu J, Li J, Chu H. Chemically grafted Nanozyme Composite cryogels to enhance antibacterial and biocompatible performance for Bioliquid Regulation and adaptive Bacteria trapping. ACS Nano. 2021;15:19672–83.
42. Li Y, Fu R, Duan Z, Zhu C. Artificial Nonenzymatic antioxidant MXene Nanosheet-Anchored Injectable Hydrogel as a mild photothermal-controlled oxygen release platform for Diabetic Wound Healing. ACS Nano. 2022;16:7486–502.
43. Ubani-Ukoma U, Gibson D, Schultz G, Silva BO, Chauhan A. Evaluating the potential of drug eluting contact lenses for treatment of bacterial keratitis using an ex vivo corneal model. Int J Pharm. 2019;565:499–508.
44. Tapola NS, Lyyra ML, Kolehmainen RM, Sarkkinen ES, Schauss AG. Safety aspects and cholesterol-lowering efficacy of chitosan tablets. J Am Coll Nutr. 2008;27:22–30.
45. Vasconcelos DP, Fonseca AC, Costa M, Amaral IF, Barbosa MA, Águas AP, Barbosa JN. Macrophage polarization following chitosan implantation. Biomaterials. 2013;34:9952–9.
46. Ji L, Zhao X, Zhang B, Kang L, Song W, Zhao B, Xie W, Chen L. X Hu. Slc6a8-Mediated Creatine Uptake and Accumulation Reprogram Macrophage polarization via regulating cytokine responses. Immunity. 2019;51:272 – 84.e7.
47. Brooks JF 2nd, Behrendt CL, Ruhn KA, Lee S, Raj P, Takahashi JS, Hooper LV. The microbiota coordinates diurnal rhythms in innate immunity with the circadian clock. Cell. 2021;184:4154-67.e12.

Publisher's note